Modified two-stream instability in the foot of high Mach number quasi-perpendicular shocks

Matsukiyo, Shuichi
Department of Earth System Science and Technology, Kyushu University | Centre for Interdisciplinary Plasma Science, Max-Planck-Institut für extraterrestrische Physik

Scholer, Manfred
Centre for Interdisciplinary Plasma Science, Max-Planck-Institut für extraterrestrische Physik | Department of Earth System Science and Technology, Kyushu University

出版情報：Journal of geophysical research. 108 (A12), pp.1459-, 2003. the American Geophysical Union
バージョン：

JOURNAL OF GEOPHYSICAL RESEARCH, VOL. ???, XXXX, DOI:10.1029/,

Modified two-stream instability in the foot of high Mach number quasi-perpendicular shocks

Shuichi Matsukiyo and Manfred Scholer

Centre for Interdisciplinary Plasma Science, Max-Planck-Institute für

Extraterrestrische Physik, Garching, Germany

Abstract.

The modified two-stream instability in the foot of supercritical quasi-perpendicular shock wave is investigated. A linear analysis shows that the instability can sufficiently grow during the shock reformation cycle for the case of a realistic ion to electron mass ratio. The wave-particle interactions of the Landau type of both the electrons and ions are essential in a finite beta plasma and lead to a reduction of the growth rate with increasing beta. The magnetic polarization in terms of wavevector is also analyzed. Additional one-dimensional full particle electromagnetic simulations in a periodic system reveal some important nonlinear wave properties: The wave spectra indicate a lower cascade due to wave-wave interactions. The parallel phase space distribution of electrons correlates well with the wave profile of the magnetic field component perpendicular to both the ambient magnetic field and the wavevector. The nonlinearly generated waves lead to electron heating parallel to the magnetic field.

1. Introduction

In the transition region of collisionless shocks numerous instabilities can get excited. In particular, it has been recognized that in high Mach number quasi-perpendicular supercritical shocks specularly reflected ions play an essential role in the wave excitation mechanisms. Recent theoretical studies have shown that the electron dynamics is inseparably related with the excitation mechanisms of the short wavelength waves. For instance, it has been suggested that the Buneman instability is excited in the foot if the relative bulk velocity between electrons and the reflected ions, u_{d}, exceeds the electron thermal velocity, v_{the}, [e.g., Papadopoulos, 1988, Cargill and Papadopoulos, 1988, Shimada and Hoshino, 2000]. The ion acoustic instability is also thought to be a candidate for a possible instability when $T_{\mathrm{e}}/T_{\mathrm{i}} \gg 1$ and u_{d} exceeds the ion acoustic speed, where T_{e} and T_{i} are the electron and ion temperatures, respectively [Papadopoulos, 1988, Cargill and Papadopoulos, 1988]. In addition, at the shock ramp a variety of instabilities, e.g., the lower-hybrid drift instability, the electron cyclotron drift instability, etc., have been theoretically investigated [see the review by Wu et al., 1984].

In addition, the so-called modified two-stream (MTS) instability is a possible candidate. This instability is driven by the relative drift between electrons and ions across the magnetic field, $\mathbf{B}_0$, even for $T_{\mathrm{e}}/T_{\mathrm{i}} \sim 1$ and $u_{\mathrm{d}} < v_{\mathrm{the}}$ [Krall and Liewer, 1971], a condition which is often satisfied in the Earth's bow shock. The MTS instability was thought to be a favorable dissipation mechanism at the ramp of the (quasi-) perpendicular subcritical shocks. Since the physical quantities, like magnetic field, density, temperature, and electrostatic (ES) potential, have significant gradients at the ramp, the relative drift between the electrons and ions is produced along the shock surface [Lashmore-Davies,

1971, Krall and Liewer, 1971, Ott et al., 1972, McBride et al., 1972, McBride and Ott, 1972, Lemons and Gary, 1978, Winske et al., 1987]. Some in situ observations at the subcritical bow shock were explained by the MTS instability of this type [Winske et al. 1987]. In contrast, for the supercritical shocks, the relative ion drift to the electrons arises in the direction parallel to the shock normal because of the presence of specularly reflected ions. This relative drift can also be the free energy for the MTS instability [Wu et al., 1984, Wu et al., 1983, Gary et al., 1987]. Scudder et al. [1986] gave comparison between linear theory of this instability and the ISEE spacecraft data at the bow shock. Recently, Scholer et al. [2003] reproduced the MTS instability of the latter type in the foot of a quasi-perpendicular supercritical shocks by performing shock simulations with a one-dimensional full particle code. They showed that the instability can grow sufficiently during the shock reformation cycle if a realistic ion to electron mass ratio is assumed.

Although a number of studies on this instability have been reported, some important points are still unresolved. Wu et al., [1983] pointed out the importance of kinetic effects of the MTS instability (they termed it kinetic cross-field streaming instability). However, they did not investigate kinetic effects in any detail. The polarization of the generated waves has also not been discussed thoroughly. It is known that the waves propagate almost perpendicular to B_0, and that the ratio of ES to EM (electromagnetic) electric field energy is very large. But, the energy of the magnetic field fluctuation is comparable to that of the ES field fluctuation [Lemons and Gary, 1977]. In this respect, it is useful to discuss magnetic polarization in terms of the wavevector. The nonlinear development of the instability has also been examined by many authors [Ott et al., 1972, McBride et al., 1972, Winske et al., 1985, Winske et al., 1987, Yoon and Lui, 1993]. For example, Ott et al.

[1972] and McBride et al. [1972] showed that in the low beta case the unstable waves heat the electrons parallel to B_0 and ions perpendicular to B_0 comparably. Later, Winske et al. [1985] revealed that ion heating becomes more isotropic and electron heating becomes more concentrated in the parallel direction as beta increases. However, most of these past studies did not mention the characteristics of the nonlinear waves. This is expected to be very important when interpreting observational data. Therefore, the purpose of this study is to investigate the MTS instability as it applies to the foot of quasi-perpendicular shocks in more detail. In particular, the parameters used in the numerical calculations are applicable to the foot of a supercritical quasi-perpendicular terrestrial bow shock.

In next section, the linear dispersion relation is derived, and the kinetic effects and the magnetic polarization are discussed. In section 3, the results of one-dimensional full particle simulation of the instability in a homogeneous system with realistic mass ratio are shown and the nonlinear wave characteristics are presented. A Summary and Discussion is given in section 4.

2. Dispersion Relation

During the shock reformation, the bulk velocity of the ions in the foot decreases because some ($20 \sim 30\%$) of the incoming ions are reflected at the shock front. Then, requiring zero current in the shock normal direction, the electron bulk velocity should also decrease in the foot. As a result, a finite difference of the bulk velocities between the electrons and the incoming/reflected ions arises. Such a velocity difference can be the source of instabilities. Although the velocity difference between the incoming and the reflected ions can also drive ion-ion instabilities [Biskamp and Welter, 1972], our discussion here is restricted to the instabilities based on the electron-ion interaction.

In the following, we adopt the coordinate system in which the electrons are at rest. The waves are assumed to propagate in the $x-z$ plane, and the incoming/reflected ions drift in a direction parallel or antiparallel to the waves. The ambient magnetic field, B_0, is in the $z-$direction, and the wave propagation angle to B_0 is θ. Since we consider waves with much higher frequencies than the ion gyrofrequency (or with much smaller wavelength than the ion gyroradius) the ions are assumed to be unmagnetized. The distribution functions of each plasma component are given by a (shifted-) Maxwellian:

$$f_{0\mathsf{j}}(v_\parallel, v_\perp) = \frac{n_{0\mathsf{j}}}{(\pi)^{3/2} v_{\mathsf{thj}}^{3/2}} \exp\left(-\frac{(v_\parallel - u_\mathsf{j})^2}{v_{\mathsf{thj}}^2} - \frac{v_\perp^2}{v_{\mathsf{thj}}^2}\right), \tag{1}$$

where $v_\parallel$ and $v_\perp$ are velocities parallel and perpendicular to the wave propagation direction, $n_{0\mathsf{j}}$ the density, $v_{\mathsf{thj}}^2 = 2\square T_\mathsf{j}/m_\mathsf{j}$ the thermal velocity ($\square$ indicates the Boltzmann constant, T_j is the temperature and m_j is the mass), and u_j is the drift velocity, respectively. The subscript j denotes particle species ($j = e, i, r$ for the electrons, the incoming ions, and the reflected ions, respectively).

After the standard procedure of linearization, the following relation is obtained [e.g., Stix, 1992].

$$\begin{pmatrix} \epsilon_{\mathsf{xx}} - N^2\cos^2\theta & \epsilon_{\mathsf{xy}} & \epsilon_{\mathsf{xz}} + N^2\cos\theta\sin\theta \\ \epsilon_{\mathsf{yx}} & \epsilon_{\mathsf{yy}} - N^2 & \epsilon_{\mathsf{yz}} \\ \epsilon_{\mathsf{zx}} + N^2\cos\theta\sin\theta & \epsilon_{\mathsf{zy}} & \epsilon_{\mathsf{zz}} - N^2\sin^2\theta \end{pmatrix} \begin{pmatrix} E_\mathsf{x} \\ E_\mathsf{y} \\ E_\mathsf{z} \end{pmatrix} = 0, \tag{2}$$

where $N^2 = c^2k^2/\omega^2$ (c indicates the light speed, k and ω denote the wavenumber and the frequency of the wave, respectively), and $\epsilon_{\mathsf{lm}} = \mathsf{1} + \sum_\mathsf{j} \chi_{\mathsf{j,lm}}$ represents the components of the dielectric tensor. Here, the elements of susceptibility tensor are as follows.

$$
\begin{aligned}
\chi_{\mathrm{e,xx}} &= C_{\mathrm{e1}}(1-\lambda_{\mathrm{e}})[Z(\zeta_{\mathrm{e},+1})+Z(\zeta_{\mathrm{e},-1})],\\
\chi_{\mathrm{e,yy}} &= C_{\mathrm{e1}}\{4\lambda_{\mathrm{e}}Z(\zeta_{\mathrm{e},+1})+(1-3\lambda_{\mathrm{e}})[Z(\zeta_{\mathrm{e},+1})+Z(\zeta_{\mathrm{e},-1})]\},\\
\chi_{\mathrm{e,zz}} &= C_{\mathrm{e2}}\{2\omega(1-\lambda_{\mathrm{e}})[1+\zeta_{\mathrm{e},0}Z(\zeta_{\mathrm{e},+1})]\\
&\quad +\lambda_{\mathrm{e}}[(\omega+\Omega_{\mathrm{e}})(1+\zeta_{\mathrm{e},+1}Z(\zeta_{\mathrm{e},+1}))+(\omega-\Omega_{\mathrm{e}})(1+\zeta_{\mathrm{e},-1}Z(\zeta_{\mathrm{e},-1}))]\},\\
\chi_{\mathrm{e,xy}} &= iC_{\mathrm{e1}}(1-2\lambda_{\mathrm{e}})[Z(\zeta_{\mathrm{e},+1})-Z(\zeta_{\mathrm{e},-1})]=-\chi_{\mathrm{e,yx}},\\
\chi_{\mathrm{e,xz}} &= C_{\mathrm{e3}}(1-\lambda_{\mathrm{e}})[\zeta_{\mathrm{e},+1}Z(\zeta_{\mathrm{e},+1})-\zeta_{\mathrm{e},-1}Z(\zeta_{\mathrm{e},-1})]=\chi_{\mathrm{e,zx}},\\
\chi_{\mathrm{e,yz}} &= iC_{\mathrm{e3}}\{(2-3\lambda_{\mathrm{e}})[1+\zeta_{\mathrm{e},0}Z(\zeta_{\mathrm{e},0})]\\
&\quad -(1-2\lambda_{\mathrm{e}})[2+\zeta_{\mathrm{e},+1}Z(\zeta_{\mathrm{e},+1})+\zeta_{\mathrm{e},-1}Z(\zeta_{\mathrm{e},-1})]\}=-\chi_{\mathrm{e,zy}},\\
\chi_{\mathrm{i,xx}} &= C_{\mathrm{i1}}\zeta_{\mathrm{i},0}Z(\zeta_{\mathrm{i},0})\cos^2\theta+C_{\mathrm{i2}}[1+\zeta_{\mathrm{i},0}Z(\zeta_{\mathrm{i},0})]\sin^2\theta,\\
\chi_{\mathrm{i,yy}} &= C_{\mathrm{i1}}\zeta_{\mathrm{i},0}Z(\zeta_{\mathrm{i},0}),\\
\chi_{\mathrm{i,zz}} &= C_{\mathrm{i1}}\zeta_{\mathrm{i},0}Z(\zeta_{\mathrm{i},0})\sin^2\theta+C_{\mathrm{i2}}[1+\zeta_{\mathrm{i},0}Z(\zeta_{\mathrm{i},0})]\cos^2\theta,\\
\chi_{\mathrm{i,xz}} &= \{-C_{\mathrm{i1}}\zeta_{\mathrm{i},0}Z(\zeta_{\mathrm{i},0})+C_{\mathrm{i2}}[1+\zeta_{\mathrm{i},0}Z(\zeta_{\mathrm{i},0})]\}\sin\theta\cos\theta=\chi_{\mathrm{i,zx}},\\
\chi_{\mathrm{i,xy}} &= \chi_{\mathrm{i,yx}}=\chi_{\mathrm{i,yz}}=\chi_{\mathrm{i,zy}}=0,
\end{aligned}
\tag{3}
$$

where $C_{\mathrm{e1}}=\omega_{\mathrm{pe}}^2/2\omega k_{\parallel}v_{\mathrm{the}}$, $C_{\mathrm{e2}}=\omega_{\mathrm{pe}}^2/\omega k_{\parallel}^2v_{\mathrm{the}}^2$, $C_{\mathrm{e3}}=\omega_{\mathrm{pe}}^2k_{\perp}/2\omega\Omega_{\mathrm{e}}k_{\parallel}$, $C_{\mathrm{i1}}=\omega_{\mathrm{pi}}^2/\omega^2$, $C_{\mathrm{i2}}=2\omega_{\mathrm{pi}}^2/k^2v_{\mathrm{thi}}^2$, $\lambda_{\mathrm{e}}=k_{\perp}^2v_{\mathrm{the}}^2/2\Omega_{\mathrm{e}}^2$, $\zeta_{\mathrm{e,n}}=(\omega+n\Omega_{\mathrm{e}})/k_{\parallel}v_{\mathrm{the}}$ $(n=0,\pm1)$, $\zeta_{\mathrm{i},0}=(\omega-ku_{\mathrm{i}})/kv_{\mathrm{thi}}$, and Z is the so-called plasma dispersion function. $k_{\parallel}=k\cos\theta$, $k_{\perp}=k\sin\theta$, $\omega_{\mathrm{pj}}^2=4\pi n_{0\mathrm{j}}e^2/m_{\mathrm{j}}$, and $\Omega_{\mathrm{e}}=eB_0/m_{\mathrm{e}}c$. In deriving the above equation, the contribution from the electron cyclotron higher harmonics $(n=\pm2,\pm3,\cdots)$ are neglected. The susceptibility tensor of the reflected ions is given by replacing the subscript i with r. However, since we focus here on the interaction between the electrons and ions, it is sufficient if only one ion component is considered. Therefore, we discuss hereafter the case for $\omega_{\mathrm{pr}}=0$ for simplicity. The dispersion relation is given by putting the determinant of the above matrix coefficient to zero.

2.1. Asymptotic Solutions for Cold Plasma

Let us discuss some asymptotic solutions of the dispersion relation. In the case that $N^2\gg1$, $\omega_{\mathrm{pi}}^2/k^2c^2\ll1$, and a cold plasma $(v_{\mathrm{the}}=v_{\mathrm{thi}}=0)$, the dispersion relation is simplified as follows:

$$
\left(1-\frac{\omega_{\mathrm{pi}}^2}{(\omega-ku_{\mathrm{i}})^2}-\frac{\omega_{\mathrm{pe}}^2}{\omega^2}\right)\left(1-\frac{\Omega_{\mathrm{e}}^2\cos^2\theta}{\omega^2(1+H_{\mathrm{e}})^2}\right)-\frac{\Omega_{\mathrm{e}}^2\sin^2\theta}{\omega^2(1+H_{\mathrm{e}})}\left(1-\frac{\omega_{\mathrm{pi}}^2}{(\omega-ku_{\mathrm{i}})^2}\right)=0, \tag{4}
$$

where $H_e = \omega_{pe}^2/k^2c^2$. It is easily found that the ES and the EM oscillations are decoupled when $\theta = 0$. In this case the ion beam can generate only the ES plasma oscillation through the Buneman instability, while the EM whistler wave is stable. However, if θ is finite, the ion beam can interact also with the whistler waves. If we assume $\omega_{pe}^2 \gg \Omega_e^2 > \omega^2$, and $\omega = \omega_0 + \omega_1 (|\omega_0| \gg |\omega_1|)$, then we obtain

$$\frac{\omega_0}{\Omega_i} = \frac{\mu \cos\theta}{\sqrt{1+H_e}} \left[\frac{\tau}{\tau(1+H_e)+\sin^2\theta}\right]^{1/2} \left(= \frac{ku_i}{\Omega_i}\right), \tag{5}$$

$$\frac{\delta_{max}}{\Omega_i} = \frac{\sqrt{3}\mu^{2/3}}{2} \left(\frac{\cos\theta \sin^2\theta}{2\sqrt{1+H_e}}\right)^{1/3} \left[\frac{\tau}{\tau(1+H_e)+\sin^2\theta}\right]^{1/2}, \tag{6}$$

where $\Omega_i = eB_0/m_ic$, $\mu = m_i/m_e$, $\tau = \omega_{pe}^2/\Omega_e^2$, and $\delta_{max} = Im[\omega_1]$. This is the MTS instability. Figure 1 represents the solution of (4) for, $\mu = 100$, $\theta = 60°$, $\tau = 4$, and $u_i/v_A = 1$. The upper/lower panel shows the real/imaginary part of the frequency as a function of wavenumber. The whistler wave is actually unstable, although the Buneman instability is dominant for this parameter regime (the electrons are cold). In this paper, we restrict ourselves to the MTS instability. The possibility of the Buneman instability taking place will be discussed in the discussion section.

Figure 2 shows the μ dependence of the maximum growth rate, δ_{max}, for $\theta = 85°$, $u_i/v_A = 2$, and $\tau = 10$ and 2×10^4. Note that δ_{max} strongly depends on μ, while the τ dependence is not significant. This characteristics is common for a wide parameter range. If m_e is fixed, the dispersion relation of the whistler wave and the ion beam velocity are almost independent of μ. But the normalization factors Ω_i (to δ_{max}) and v_A (to the ion beam velocity, u_i) have a μ dependence. As a result, δ_{max}/Ω_i varies as $\sim \mu^{2/3}$ [see (6)]. Therefore, when the mass ratio has the realistic value ($\mu = 1836$), the growth rate is large enough compared to the ion gyrofrequency, which characterizes the shock reformation

cycle. In other words, if μ is nonrealistically small ($\mu < 1836$), as assumed in most full particle simulations of collisionless shocks, it is difficult to obtain this instability in the foot region.

The MTS instability is stabilized if $u_{\mathsf{i}}/v_{\mathsf{A}}$ exceeds the maximum phase velocity of whistler wave, which is obtained as $\omega/kv_{\mathsf{A}} \approx \mu^{1/2}\cos\theta/2$ for $\tau \gg 1$. Here, we should note that this instability can also be excited through an interaction between electrons and reflected ions. From the zero current condition in the shock normal direction, a relative bulk velocity between electrons and reflected ions is obtained as $|\Delta u_{\mathsf{re}}|/v_{\mathsf{A}} = 2(1-\alpha)M_{\mathsf{A}}$, while a relative bulk velocity between electrons and incoming ions is given by $\Delta u_{\mathsf{ie}}/v_{\mathsf{A}} = 2\alpha M_{\mathsf{A}}$, where α is the ratio of reflected to total ion number densities and M_{A} denotes the Alfvén Mach number. Therefore, the MTS instability can be driven if

$$\cos\theta > \frac{4(1-\alpha)M_{\mathsf{A}}}{\sqrt{\mu}} \tag{7}$$

by the electron-reflected ion interaction, and if

$$\cos\theta > \frac{4\alpha M_{\mathsf{A}}}{\sqrt{\mu}} \tag{8}$$

by the electron-incoming ion interaction, respectively. Typically $\alpha \sim 0.2$, so that the instability of latter type can be destabilized in a wider range of θ compared to the instability of the former type. Gary et al. [1987] showed, however, that the maximum growth rate of the former type is greater than that of the latter type for low beta. Nevertheless, we restrict our discussion to the instability of the latter type hereafter, since one of the aims of this paper is to give a more precise interpretation of the waves observed by Scholer et al. [2003] who found the instability of this type in their shock simulations. The characteristics of both types of the MTS instability are similar in many way.

2.2. Solutions for Hot Plasma

The instability is suppressed not only by assuming nonrealistic μ but also by kinetic effects due to finite temperature [Wu et al., 1983, Gary et al., 1987]. In order to discuss kinetic effects, we solve in the following the complete dispersion relation, i.e., we determine the zero determinant of the matrix coefficients of (2).

Figure 3(a) represents a contour plot of the growth rate in $\beta_e(\beta_i) - kc/\omega_{pe}$ space. The parameters are $\mu = 1836$, $\theta = 85°$, $\tau = 2 \times 10^4$, and $u_i/v_A = 2$. The last two parameters correspond to the parameters in the foot of Earth's bow shock with $M_A = 4$ and $\alpha = 0.25$. It is obvious that the growth rate decreases as $\beta_e(\beta_i)$ increases. To identify the dominant kinetic effects, the growth rates (upper panel) and the real parts of ζ^{-1} (lower panel) are shown in Figure 4(a) for the same parameters as above. The dashed lines correspond to the case for $\beta_e = \beta_i = 0$, the dotted lines for $\beta_e = 0.25$ and $\beta_i = 0$, and the solid lines for $\beta_e = \beta_i = 0.25$, respectively. In the lower panel, it can be seen that $Re[|\zeta^{-1}_{e,\pm 1}|] \ll 1$ which indicates that the electron cyclotron damping is less important (the dotted lines for $\beta_e = 0.25$ and $\beta_i = 0$ are almost degenerate with the solid lines). In contrast, electron Landau damping is essential for $\beta_e = 0.25$ because $Re[\zeta^{-1}_{e,0}] \sim 1$. Furthermore, the kinetic effect of the ions is also quite important in the case of $\beta_e = \beta_i = 0.25$. This is because the positive slope of the ion distribution function decreases as β_i increases. This is consistent with the simulation result obtained by Scholer et al. [2003], who showed that the MTS instability is not found in their full particle shock simulation (their run 8) for the high beta medium Mach number case. Figure 3(b) again shows the contour plot of the growth rate with the same parameters as Figure 3(a) but $\theta = 70°$. Although the growth rate in the cold limit is greater than that for $\theta = 85°$, the damping is significant for finite β_e and

β_i. Figure 4(b) indicates the maximum growth rates as a function of β_e ($= \beta_i$) for the same parameters as Figure 3(b). The solid line with circles denotes a case taking both the electron and the ion kinetic effects into account, while the dotted line with triangles corresponds to a case including only the electron kinetic effects, i.e., $\beta_i = 0$. The dashed line shows the maximum growth rate of a cold plasma ($\beta_e = \beta_i = 0$). It is found that in this parameter regime the electron kinetic effects, mainly electron Landau damping, largely prevents wave growth.

2.3. Polarization in the Plane Perpendicular to k

It is useful to discuss the polarization of the magnetic field in terms of the wavevector $\mathbf{k}$ as mentioned in the Introduction. If we adopt the coordinate system shown in Figure 5, where the wavevector is parallel to the $x'-$axis and $\mathbf{B}_0$ is in the $x'-z'$ plane, the following relation is satisfied.

$$\frac{E'_z}{E_x} = \frac{E_z}{E_x}\sin\theta - \cos\theta, \tag{9}$$

$$\frac{E'_y}{E_x} = \frac{E_y}{E_x}, \tag{10}$$

where

$$\frac{E_z}{E_x} = \frac{D_{xy}D_{yx} - D_{yy}D_{xx}}{D_{xy}D_{yz} - D_{yy}D_{xz}}, \tag{11}$$

$$\frac{E_y}{E_x} = -\frac{D_{xx}}{D_{xy}} - \frac{D_{xz}}{D_{xy}}\frac{E_z}{E_x}. \tag{12}$$

In the above, D_{ij} indicates each component of the matrix coefficient in (2). The polarization of the magnetic fluctuation is defined as

$$\left|\frac{B'_y}{B'_z}\right| = \left|\frac{E'_z}{E'_y}\right|. \tag{13}$$

This polarization at the maximum growth rate is shown in Figure 6 for $\tau = 2 \times 10^4$, $\mu = 1836$, $u_{\mathsf{i}}/v_{\mathsf{A}} = 2$, and $\theta = 85^\circ$. $|B'_{\mathsf{y}}/B'_{\mathsf{z}}| \gtrsim 1$ in a wide range of β_{e} $(= \beta_{\mathsf{i}})$. The numerical solutions show that for these parameters (13) is approximately written as $|B'_{\mathsf{y}}/B'_{\mathsf{z}}| = |(D_{\mathsf{xx}}/D_{\mathsf{xz}})\sin\theta + \cos\theta|/|D_{\mathsf{yx}}/D_{\mathsf{yy}}|$ for the unstable mode, and $|D_{\mathsf{yx}}|$ decreases when beta is finite while other three components of the dielectric coefficient do not vary very much. This means that the $y'-$ component of current fluctuation produced by the electron $\mathsf{E}'_{\mathsf{x}} \times \mathsf{B}_0$ drift decreases in a finite beta plasma, which leads to reduction of B'_{z}. The above characteristics holds for a wide range of θ.

3. 1-D Periodic Simulation

In addition to the linear analysis discussed above, we have performed a one-dimensional full particle simulation. Since we focus here only on the foot region of the shock a periodic boundary condition can be used, i.e., a periodic system is assumed to represent the foot region. The coordinate system used here is shown in Figure 5. For simplicity, the primes are omitted hereafter. The one-dimensionality of the system only allows waves with wavevectors in $x-$direction. We assume that the system contains three plasma components, i.e., incoming ions and electrons, and reflected ions. All plasma components are magnetized, and a motional electric field is absent because the simulation is performed in the electron frame of reference.

Because of restrictions in simulation time we use an unrealistically low value of $\tau = 10$. This should not seriously affect the result of the instability as noted in section 2.1. Other parameters are $\mu = 1836$, $\theta = 85^\circ$, $u_{\mathsf{i}}/v_{\mathsf{A}} = 2.0$, $u_{\mathsf{r}}/v_{\mathsf{A}} = -6.0$, $\beta_{\mathsf{e}} = 0.1$, $\beta_{\mathsf{i}} + \beta_{\mathsf{r}} = 0.1$, $\alpha = 0.25$, and the system length is $102.4c/\omega_{\mathsf{pe}}$. In a one-dimensional simulation with above parameters, the reflected ions do not contribute strongly to the instability but

just neutralize the charge and the zero-th order current. The simulation is done with 8192 spatial grid points, the number of particles for each specie is 100 per cell, and $\omega_{pe}\Delta t = 0.0125$.

3.1. Spectral Analysis

Figure 7 shows time evolution of the total ES field energy. The linear instability saturates at $\Omega_i t = 0.38$. During the period $0.38 < \Omega_i t < 0.55$, a clear nonlinear oscillation of the field energy due to electron trapping is seen. For $\Omega_i t > 0.55$, the system becomes more turbulent because a variety of side band waves are excited probably due to the nonlinear wave-wave interactions discussed below. Figure 8 represents the $\omega - k$ spectra of E_x and B_y fields during the time interval (a) $0 < \Omega_i t < 0.35$ and (b) $0.53 < \Omega_i t < 0.88$. Clearly, Figure 8(a) shows the characteristics of the linear stage. During this period, we observe parallel electron and perpendicular ion heating, as reported by Scholer et al. [2003]. On the other hand, in Figure 8(b), the spectra vary considerably from those of the linear stage. The characteristics of Figure 8(b) can be summarized as follows : (1) The E_x spectrum contains some waves with small phase velocity which are absent in Figure 8(a), although the waves with small phase velocity are not observed in the B_y spectrum. (2) The wave spectra show a lower cascade in k space. (3) Some higher phase velocity waves are seen in the E_x spectrum (arrowed region), and they are associated with secondary electron heating as shown later.

3.1.1. Generation of Small Phase Velocity Waves

The main reason for the small phase velocity waves to be excited is a decrease of the bulk velocity v_{ix} of the incoming ions due to their gyration. This results in a change of the dispersion relation. We confirmed that the spectral broadening is suppressed (but

not completely) if it is assumed in the simulation that the ions are demagnetized. A spreading of the particle distribution function is also responsible for the broadening of the wave spectrum. For this parameter regime, the instability is resonant ($-2 < \zeta_{i0}^{-1} < -1$ during the simulation), so that the wave phase velocity decreases in time when the position of maximum positive slope of the ion distribution function in v_{ix} decreases due to ion heating [Goldstein et al., 1978]. In contrast, such a spectral broadening is not seen in the B_y spectrum. We will show later that this is related with the electron response to the waves.

3.1.2. Spectral Cascade

The nonlinear spectral cascade was reported by McBride et al. [1972]. They indicated that the linearly generated waves strongly couple with each other in the nonlinear stage, and the wave spectrum predominantly cascades to long wavelength. Our simulation result also indicates a similar spectral cascade. In Figure 9, the wave power spectra of E_x are shown as a function of k at three different times. In the linear stage ($\Omega_i t = 0.34$), a peak of the spectrum lies at $kc/\omega_{pe} \sim 2$, as predicted by the linear theory. However, in the nonlinear stage ($\Omega_i t = 0.43, 0.69$), the spectral peak shifts to lower k, and further side band waves are amplified ($\Omega_i t = 0.69$). In the present simulation the linearly generated waves have a broad $k-$spectrum, so that there are a number of candidates for wave-wave interactions. Therefore, it is rather difficult to identify a dominant wave-wave interaction. Here, we only discuss some possible mechanisms which may be responsible for the side band waves. One of them is the decay type in which a large amplitude parent wave generates a whistler-like wave propagating in the direction opposite to the parent wave. Some negatively propagating whistler-like waves are actually seen in Figure 8(b). The

decay instability also generates another side band wave which propagates in the same direction as the parent wave but has a smaller phase velocity than the parent wave. This is another possible mechanism for producing the small phase velocity waves seen in the upper panel of Figure 8(b). If a successive decay takes place, a lower cascade would be found and both positively and negatively propagating waves would have comparable amplitudes. However, the peak intensity of the spectrum of positively propagating waves shown in Figure 8(b) is too high compared with that of the negatively propagating waves. The modulational instability is also a possible mechanism for cascading. Since all of the side band waves in this case have nearly equal phase velocities, the cascading takes place along a single line indicating approximately constant phase velocity. Other higher order correlations may be also possible.

3.1.3. High Phase Velocity Waves and Associated Electron Heating

In the nonlinear stage waves with a phase velocity larger than the incoming ion bulk velocity are generated (arrowed region in Figure 8(b)). They are close to another branch of the dispersion relation shown in Figure 1. These waves are probably excited by a nonlinear wave-wave interaction, although this is difficult to identify. Tanaka and Papadopoulos [1983] found in their simulation a nonlinear shift of the phase velocity and an associated parallel electron heating due to the MTS instability. In our simulation, additional parallel electron heating is observed as well. Figure 10 displays the electron distribution function $f(v_{ez})$ versus v_{ez} at $\Omega_i t = 0.71$. Some electrons around $v_{ez}/v_A \sim 40$ are clearly energized, which is consistent with the parallel phase velocity of the waves (a further peak at $v_{ez}/v_A \sim 14$ is the result of wave-particle interaction with linearly generated waves).

3.2. Wave Profiles and Particle Phase Space Plots

Here, we discuss wave profiles and particle phase space plots obtained by the simulation, and resolve why in the nonlinear stage the $\omega - k$ spectrum of B_y exhibits different characteristics from that of E_x as seen in Figure 8(b). Figure 11(a) shows from top to the bottom the ES potential ϕ, B_z, B_y, v_{ez}, and v_{ix} at $\Omega_i t = 0.27$. The three field components exhibit well correlated spatial structures. The amplitude of the fluctuation of B_y is almost comparable to that of B_z. These characteristics are consistent with the linear analysis. Furthermore, the electrons and ions are trapped in v_{ez} and v_{ix}, respectively. The main electric field is parallel to the $x-$direction. Since the ions are almost unmagnetized, they are trapped in v_{ix} by this E_x field. However, the electrons are strongly magnetized, so they can not move in the $x-$direction across the magnetic field. Instead, they can move freely parallel to the magnetic field and can feel the parallel electric field of the obliquely propagating waves. As a result, the electrons are trapped by this parallel electric field which is almost parallel to the $z-$direction. The above results are consistent with those obtained by Scholer et al. [2003] in full particle simulations of quasi-perpendicular shocks.

At the later time $\Omega_i t = 0.69$, the field profiles and ion and electron phase space plots exhibit larger structures, as indicated in Figure 11(b). This cascading process was discussed above. At this stage, the wave profiles of ϕ and B_z are well correlated with the ion phase space distribution, while the electron phase space distribution reflects the profile of B_y. In contrast to the profile of B_y, the ϕ and the B_z profiles contain small structures with wavelength $\lambda < 8c/\omega_{pe}$. From a spectral analysis the parallel phase velocity of these waves is roughly estimated as $\omega/k_{\parallel} v_A < 15$, which is smaller than the electron parallel thermal velocity at this time. Furthermore, the potential energy of the small wavelength

waves is about two orders of magnitude less than the electron parallel thermal energy. Therefore, the electrons can move through these small potential wells. This is the reason why the electron phase space distribution does not exhibit small structures. The parallel electron motion sustains the current fluctuation parallel to the B_0 which is almost in the $z-$direction. From Maxwell's equation, the current fluctuation in z produces B_y. Therefore, B_y correlates well with the electron phase space distribution $v_{\mathsf{ez}} - x$. The top panel of Figure 12 denotes the spatial profile of ϕ in which the small wavelength waves with $\lambda < 8c/\omega_{\mathsf{pe}}$ are subtracted from ϕ in Figure 11(b). In the lower panel, B_y is again shown for comparison. Excellent correlation is seen between these two wave profiles. Moreover, since the amplitude of ϕ in Figure 12 is of the same order as electron parallel thermal energy, some electrons can be trapped by these waves.

4. Summary and Discussion

We have investigated in this paper the MTS instability as it may occur in the foot of quasi-perpendicular supercritical shocks. The free energy source of the instability is the relative velocity between the solar wind electrons and the incoming/reflected solar wind ions parallel to the shock normal. For finite temperature, kinetic effects of the Landau type associated with both electrons and ions are important. Although they inhibit wave growth, the growth rate is still large enough compared to the ion gyrofrequency for a realistic mass ratio, highly oblique case. In such a case, the instability can sufficiently grow during a shock reformation cycle. The magnetic polarization in terms of the wavevector shows that the amplitude of B_y is of the same order as that of B_z.

In the cold plasma limit, in addition to the MTS instability, the Buneman instability can also get excited (see Figure 1). At the Earth's bow shock, $\tau \gg 1$ so that the wave frequency

of the Buneman instability is much greater than electron gyrofrequency. Hence, electrons are almost unmagnetized for this frequency regime. It is well known that the Buneman instability is strongly suppressed by electron Landau damping when the electron thermal velocity is larger than the relative bulk velocity between electrons and ions. If the current conservation is satisfied in the foot, the relative bulk velocity between reflected ions and electrons is $\Delta u_{re}/v_A = 2(1-\alpha)M_A$. Since $v_{the}/v_A = (\mu\beta_e)^{1/2}$, the Buneman instability is suppressed when $\beta_e \gtrsim 4(1-\alpha)^2 M_A^2/\mu$. With $\mu = 1836$ and $\alpha = 0.2$, this results in $\beta_e \gtrsim M_A^2/720$, what is usually satisfied at the Earth's bow shock. In other words, the Buneman instability can only be generated in sufficiently low beta or high Mach number cases [Shimada and Hoshino, 2000]. It should be pointed out that the threshold value of β_e below which the Buneman instability takes place is overestimated under unrealistically small μ. As mentioned above, on the other hand, the electron Landau damping also affects the MTS instability. However, since the electrons are magnetized in this case, the condition for strong Landau damping is given by $\omega/k_{\parallel} \sim \Delta u_{je}/\cos\theta \lesssim v_{the}$, i.e., $\beta_e \gtrsim 4(1-\alpha)^2 M_A^2/\mu\cos^2\theta$ for the electron-reflected ion interaction, and $\beta_e \gtrsim 4\alpha^2 M_A^2/\mu\cos^2\theta$ for the electron-incoming ion interaction. Therefore, the MTS instability can survive for larger values of β_e compared to the Buneman instability. As a conclusion, the MTS instability is more plausible than the Buneman instability in the foot of the Earth's bow shock.

The nonlinear evolution of the MTS instability is examined in the present paper by a one-dimensional full particle simulation with periodic boundary conditions. Since the ions are almost unmagnetized and the electrons are strongly magnetized, the electrons (ions) are trapped parallel (perpendicular) to B_0, as found by Scholer et al. [2003] in a

full particle simulation of an almost perpendicular shock with realistic mass ratio. The wave spectra indicate a lower cascade in the nonlinear stage. The wave profiles of B_y correlate well with the parallel electron phase space distribution and shows relatively large spatial structures, while the wave profiles of ϕ and B_z exhibit good correlation with ion perpendicular phase space distribution which contains also relatively small spatial structure. This is due to the fact that B_y is mainly sustained by the parallel motion of electrons whose thermal energy is large compared to the ES potential energy of the small wavelength waves. Additional parallel electron heating by the higher phase velocity waves, which are excited in the nonlinear stage, has also been observed.

Although we have discussed in this paper mainly the MTS instability based on electron-incoming ion interaction, the instability based on electron-reflected ion interaction can occur simultaneously in a system with higher spatial dimensions allowing a wider k-space. Actually, Gary et al. [1987] concluded from linear analysis that the electron-reflected ion MTS instability is dominant for the low beta case ($\beta_e \lesssim 0.5$), while the electron-incoming ion MTS instability become dominant for high beta value ($\beta_e \gtrsim 0.5$) in the foot. We confirmed a similar tendency for various values of α (they mainly considered the case $\alpha = 0.1$). Furthermore, these results do not conflict with the results shown by Scudder et al. [1986] that the MTS instability via the electron-incoming (solar wind) ion interaction predominantly generates waves seen in data observed at the high beta bow shock foot. It is expected from the above sequence that two types of the MTS instability simultaneously exist for a middle range of $\beta_e \sim 0.5$ which is often satisfied at the bow shock. Therefore, the interaction of these two instabilities will be an important subject for further investigation.

Finally, let us discuss a possibility of shock reformation due to the MTS instability. This may be possible if the majority of ions is trapped by generated waves within an ion gyroperiod. Assuming a monochromatic wave spectrum, the ion trapping frequency is written as $\omega_{ti} \sim (eEk/m_i)^{1/2}$. Hence, $\omega_{ti}/\Omega_i \sim [\mu\sqrt{\tau}(kc/\omega_{pe})(E/B_0)]^{1/2} > 1$ is required. Furthermore, in order for the majority of the ions to be trapped, the ES potential energy must exceed or at least be comparable to the kinetic energy of the majority of the ions in the wave frame. If the MTS instability is strong enough, the above conditions should be satisfied and reformation is expected to occur. Confirmation of this process requires full particle quasi-perpendicular shock simulations in the appropriate parameter regime.

Acknowledgments. We should like to thank V. Krasnosselskikh and R. Treumann for helpful discussions. We are also grateful to both referees for their helpful comments.

References

Biskamp, D., and H. Welter, Structure of the Earth's bow shock, J. Geophys. Res., 77, 6052–6059, 1972.

Cargill, P. J., and K. Papadopoulos, A mechanism for strong shock electron heating in supernova remnants, Astrophys. J., 329, L29–L32, 1988.

Gary, S. P., R. L. Toker, and D. Winske, Ion/ion and electron/ion cross-field instabilities near the lower hybrid frequency, J. Geophys. Res., 92, 10029–10038, 1987.

Goldstein, B., W. Carr, B. Rosen, and M. Seidl, Numerical simulation of the weak beam-plasma interaction, Phys. Fluids, 21, 1569–1577, 1978.

Krall, N. A., and P. C. Liewer, Low-frequency instabilities in magnetic pulses, Phys. Rev. A, 4, 2094–2103, 1971.

Lashmore-Davies, C. N., Instability in a perpendicular collisionless shock wave for arbitrary ion temperatures, Phys. Fluids, 14, 1481–1484, 1971.

Lemons, D. S., and S. P. Gary, S. P., Electromagnetic effects on the modified two-stream instability, J. Geophys. Res., 82, 2337–2342, 1977.

Lemons, D. S., and Gary, Current-driven instabilities in a laminar perpendicular shock, J. Geophys. Res., 83, 1625–1632, 1978.

McBride, J. B., E. Ott, J. P. Boris, and J. H. Orens, Theory and simulation of turbulent heating by the modified two-stream instability, Phys. Fluids, 15, 2367–2383, 1972.

McBride, J. B., and E. Ott, Electromagnetic and finite β_e effects on the modified two-stream instability, Phys. Lett., 39A, 363–364, 1972.

Ott, E., J. B. McBride, J. H. Orens, and J. P. Boris, Turbulent heating in computer simulations of the modified plasma two-stream instability, Phys. Rev. Lett., 28, 88–91, 1972.

Papadopoulos, K., Electron heating in superhigh Mach number shocks, Astrophys. Space Sci., 144, 535–547, 1988.

Scholer, M., I. Shinohara, and S. Matsukiyo, Quasi-perpendicular shocks: length scale of the cross-shock potential, shock reformation, and implication for shock surfing, J. Geophys. Res., 108, doi:10.1029/2002JA009515, 2003.

Scudder, J. D., A. Mangeney, C. Lacombe, C. C. Harvey, C. S. Wu, and R. R. Anderson, The resolved layer of a collisionless, high β, supercritical, quasi-perpendicular shock wave 3. Vlasov electrodynamics, J. Geophys. Res., 91, 11075–11097, 1986.

Shimada, N., and M. Hoshino, Strong electron acceleration at high Mach number shock waves: simulation study of electron dynamics, Astrophys. J., 543, L67–L71, 2000.

Stix, T. H.,, Waves in plasmas, chap. 10, American Institute of Physics, New York, 1992.

Tanaka, M., and K. Papadopoulos, Creation of high-energy electron tails by means of the modified two-stream instability, Phys. Fluids, 26, 1697–1699, 1983.

Winske, D., M. Tanaka, C. S. Wu, and K. B. Quest, Plasma heating at collisionless shocks due to the kinetic cross-field streaming instability, J. Geophys. Res., 90, 123–136, 1985.

Winske, D., J. Giacalone, M. F. Thomsen, and M. M. Mellott, A comparative study of plasma heating by ion acoustic and modified two-stream instabilities at subcritical quasi-perpendicular shocks, J. Geophys. Res., 92, 4411–4422, 1987.

Wu, C. S., Y. M. Zhou, S. T. Tsai, S. C. Guo, D. Winske, and K. Papadopoulos, A kinetic cross-field streaming instability, Phys. Fluids, 26, 1259–1267, 1983.

Wu, C. S., D. Winske, Y. M. Zhou, S. T. Tsai, P. Rodoriguez, M. Tanaka, K. Papadopoulos, K. Akimoto, C. S. Lin, M. M. Leroy, and C. C. Goodrich, Microinstabilities associated with a high Mach number perpendicular bow shock, Space Sci. Rev., 36, 64–109, 1984.

Yoon, P. H., and A. T. Y. Lui, Nonlinear analysis of generalized cross-field current instability, Phys. Fluids B, 5, 836–853, 1993.

Figure 1. Dispersion relation in the cold plasma limit. The parameters are $\tau = 4$, $\mu = 100$, $u_i/v_A = 1$, and $\theta = 60^\circ$. The upper and lower panels show the real and imaginary parts of the frequency, respectively, as a function of wavenumber.

Figure 2. Mass ratio dependence of the maximum growth rate of the modified two-stream instability for $u_i/v_A = 2$, $\theta = 85^\circ$ and two values of τ.

Figure 3. Contour plots of the growth rate in $\beta_e(\beta_i) - kc/\omega_{pe}$ space. The parameters are $\tau = 2 \times 10^4$, $\mu = 1836$, $u_i/v_A = 2$, and (a) $\theta = 85^\circ$ and (b) $\theta = 70^\circ$.

Figure 4. Kinetic effects of the instability. (a) The growth rates (upper panel) and the $Re[\zeta^{-1}]$ (lower panel) are represented for the same parameters as in Figure 3(a). The three different lines correspond to the case $\beta_e = \beta_i = 0$ (dashed lines), $\beta_e = 0.25$ and $\beta_i = 0$ (dotted lines), and $\beta_e = \beta_i = 0.25$ (solid lines), respectively. (b) The maximum growth rates as a function of β_e $(= \beta_i)$ for the same parameters as Figure 3(b). The three different lines indicate the case $\beta_e = \beta_i = 0$ (dashed line), $\beta_e \neq 0, \beta_i = 0$ (dotted line with triangles), and $\beta_e = \beta_i \neq 0$ (solid line with circles), respectively.

Figure 5. Coordinate system used in the calculation of the magnetic polarization and in the numerical simulation.

Figure 6. Polarization of the magnetic field fluctuation in terms of wavevector as a function of $\beta_e (= \beta_i)$. The parameters are $\tau = 2 \times 10^4$, $\mu = 1836$, $u_i/v_A = 2$, and $\theta = 85^\circ$.

Figure 7. Time history of total ES field energy obtained by the simulation.

Figure 8. $\omega - k$ spectra of E_x (upper panel) and B_y (lower panel) fields for (a) $0 < \Omega_i t < 0.35$, and (b) $0.53 < \Omega_i t < 0.88$.

Figure 9. Wave power spectra for E_x at $\Omega_i t = 0.34$ (top panel), $\Omega_i t = 0.43$ (middle panel), and $\Omega_i t = 0.69$ (bottom panel).

Figure 10. Electron parallel distribution function at $\Omega_i t = 0.71$.

Figure 11. Wave profiles and particle phase space plots obtained by the simulation at (a) $\Omega_i t = 0.27$, and (b) $\Omega_i t = 0.69$.

Figure 12. Profile of ϕ (upper panel) in which the small wavelength waves with $\lambda < 8c/\omega_{pe}$ are subtracted from the data at $\Omega_i t = 0.69$. Profile of B_y is shown in the lower panel for comparison.

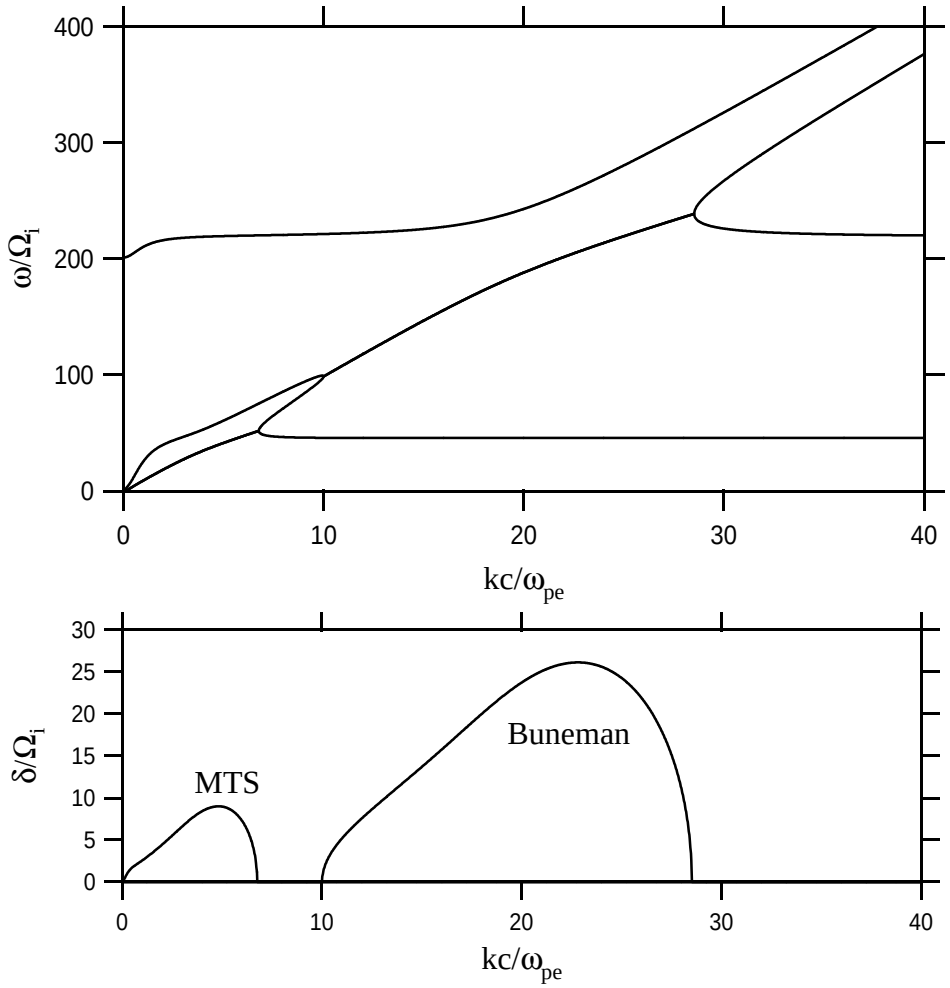
400
300
200
100
0
ω/Ω_i
0
10
20
30
40
kc/ω_pe
30
25
20
15
10
5
0
δ/Ω_i
MTS
Buneman
0
10
20
30
40
kc/ω_pe

Figure 1

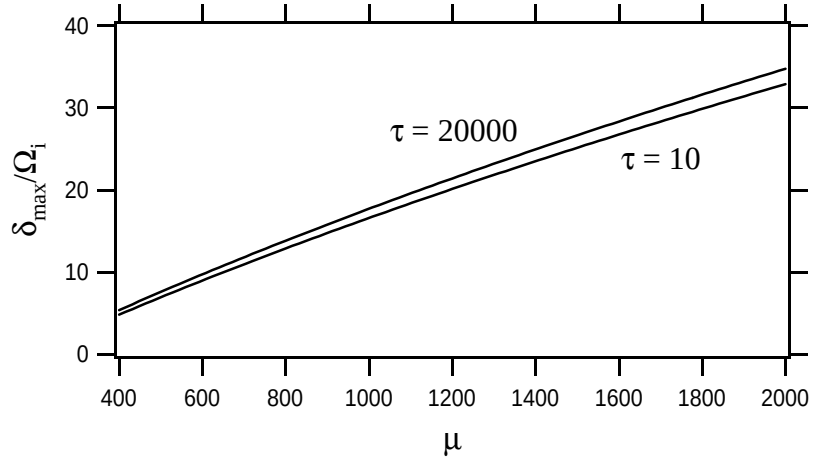
40
30
20
10
0
400
600
800
1000
1200
1400
1600
1800
2000
τ = 20000
τ = 10
δmax/Ωi
μ

Figure 2

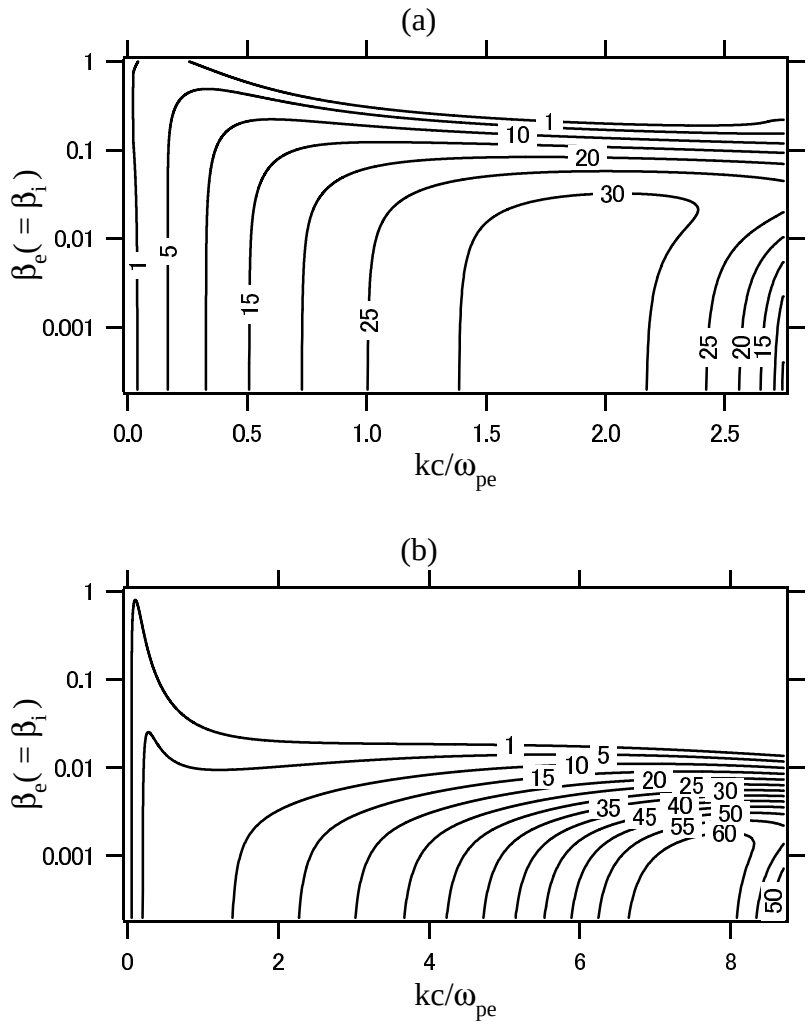
(a)
1
0.1
0.01
0.001
$\beta_e (= \beta_i)$
1
10
20
30
1
5
15
25
25
20
15
0.0
0.5
1.0
1.5
2.0
2.5
kc/ω_{pe}
(b)
1
0.1
0.01
0.001
$\beta_e (= \beta_i)$
1
5
10
15
20
25
30
35
40
45
50
55
60
50
0
2
4
6
8
kc/ω_{pe}

Figure 3

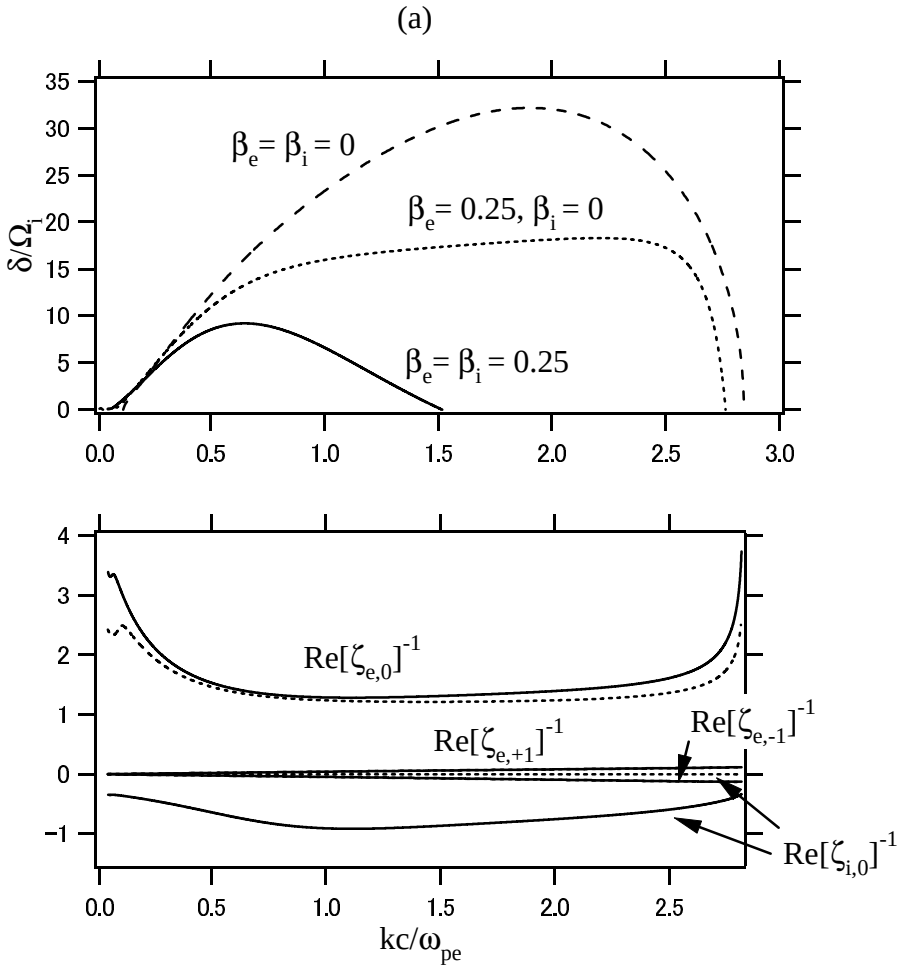
(a)
δ/Ω_i
$\beta_e = \beta_i = 0$
$\beta_e = 0.25, \beta_i = 0$
$\beta_e = \beta_i = 0.25$
$\mathrm{Re}[\zeta_{e,0}]^{-1}$
$\mathrm{Re}[\zeta_{e,+1}]^{-1}$
$\mathrm{Re}[\zeta_{e,-1}]^{-1}$
$\mathrm{Re}[\zeta_{i,0}]^{-1}$
kc/ω_{pe}
(b)
δ_{max}/Ω_i
$\beta_e (= \beta_i)$

Figure 4

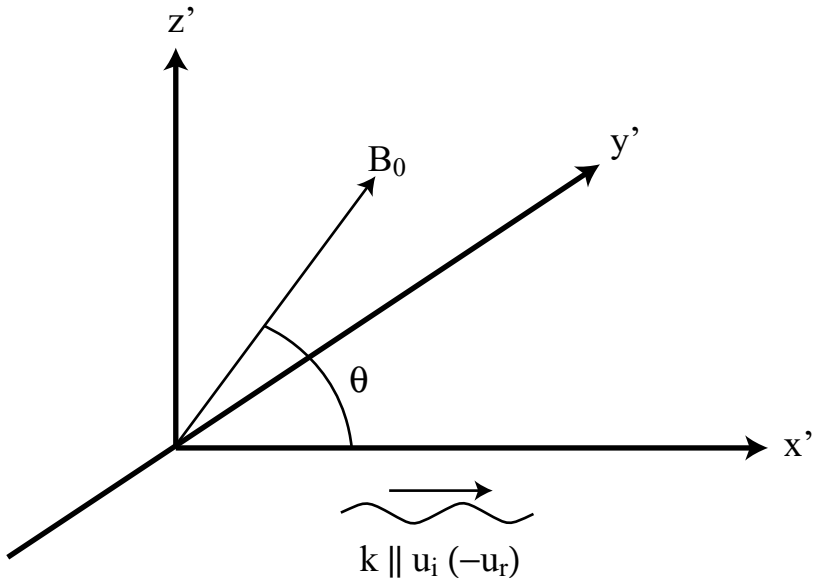

Figure 5

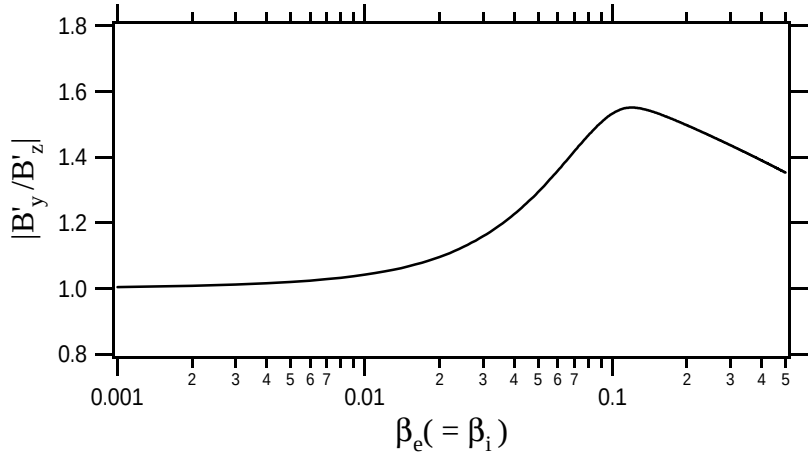

Figure 6

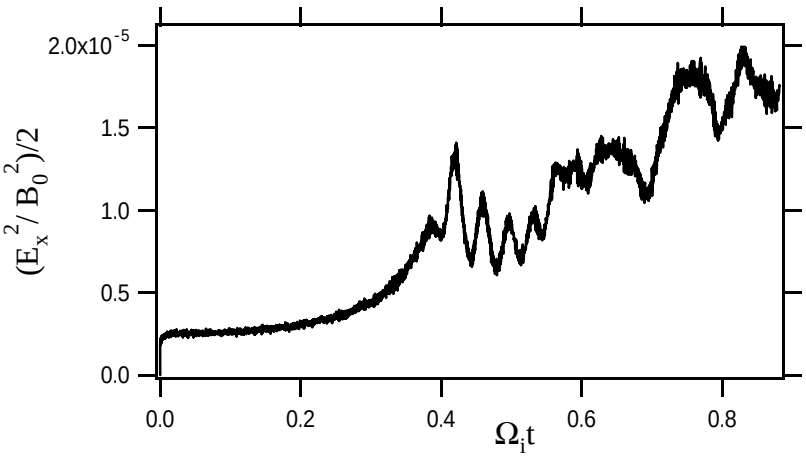

Figure 7

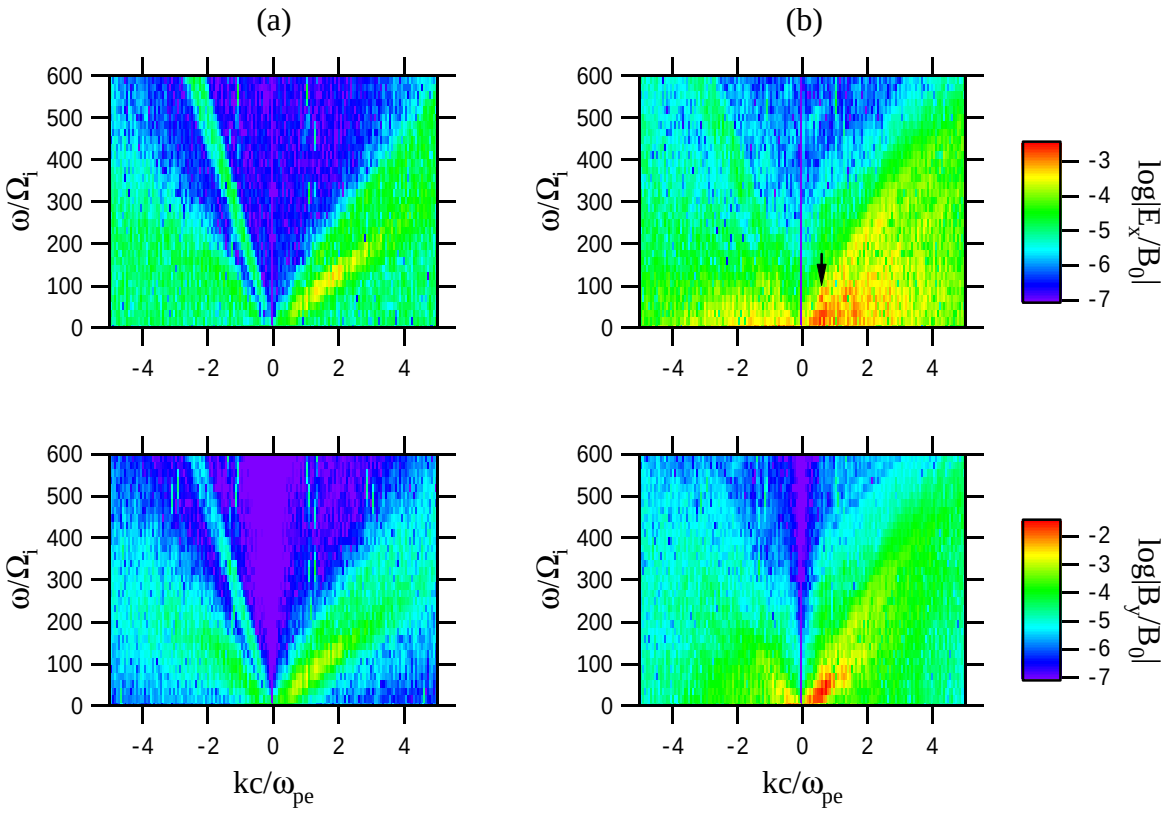

Figure 8

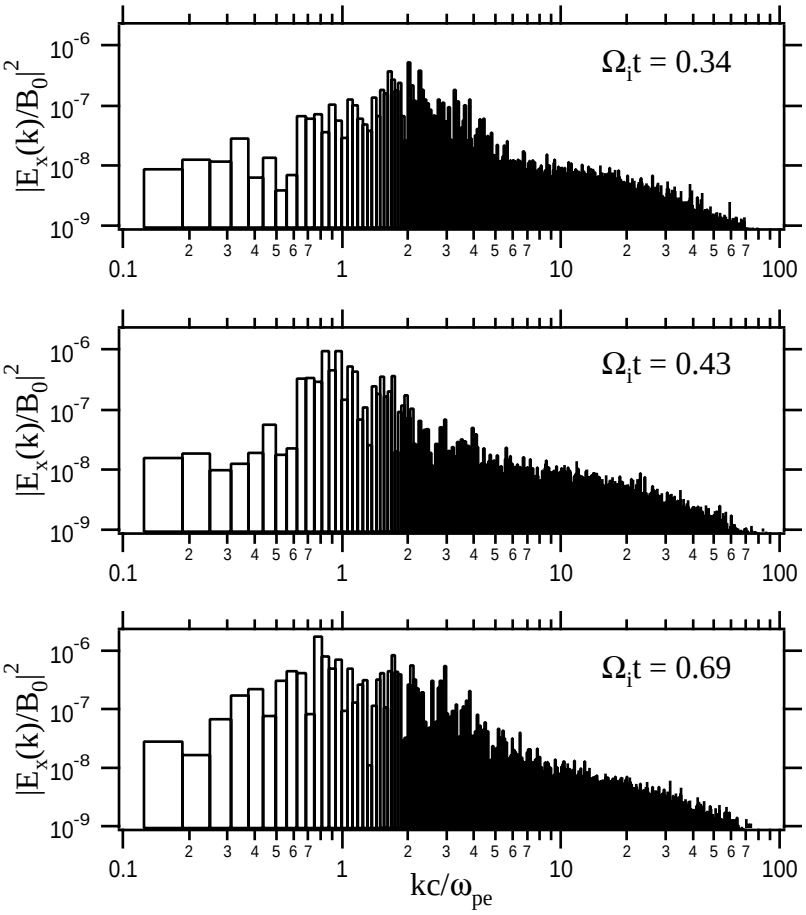
$|E_x(k)/B_0|^2$
10^{-6}
10^{-7}
10^{-8}
10^{-9}
$\Omega_i t = 0.34$
$\Omega_i t = 0.43$
$\Omega_i t = 0.69$
0.1
1
10
100
2 3 4 5 6 7
kc/ω_{pe}

Figure 9

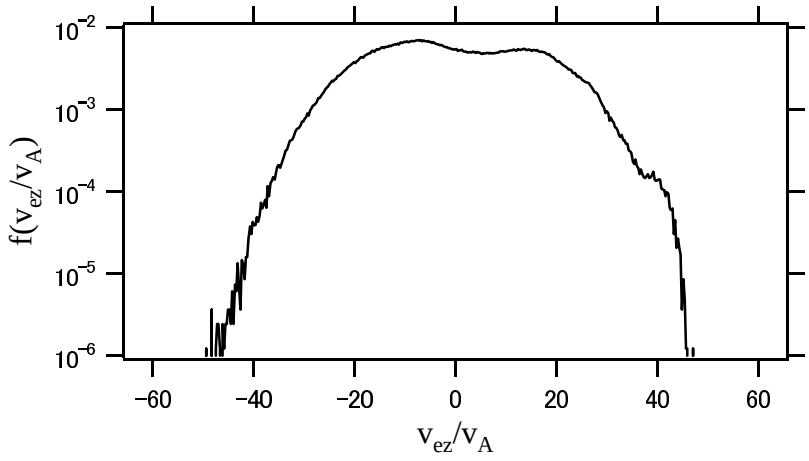

Figure 10

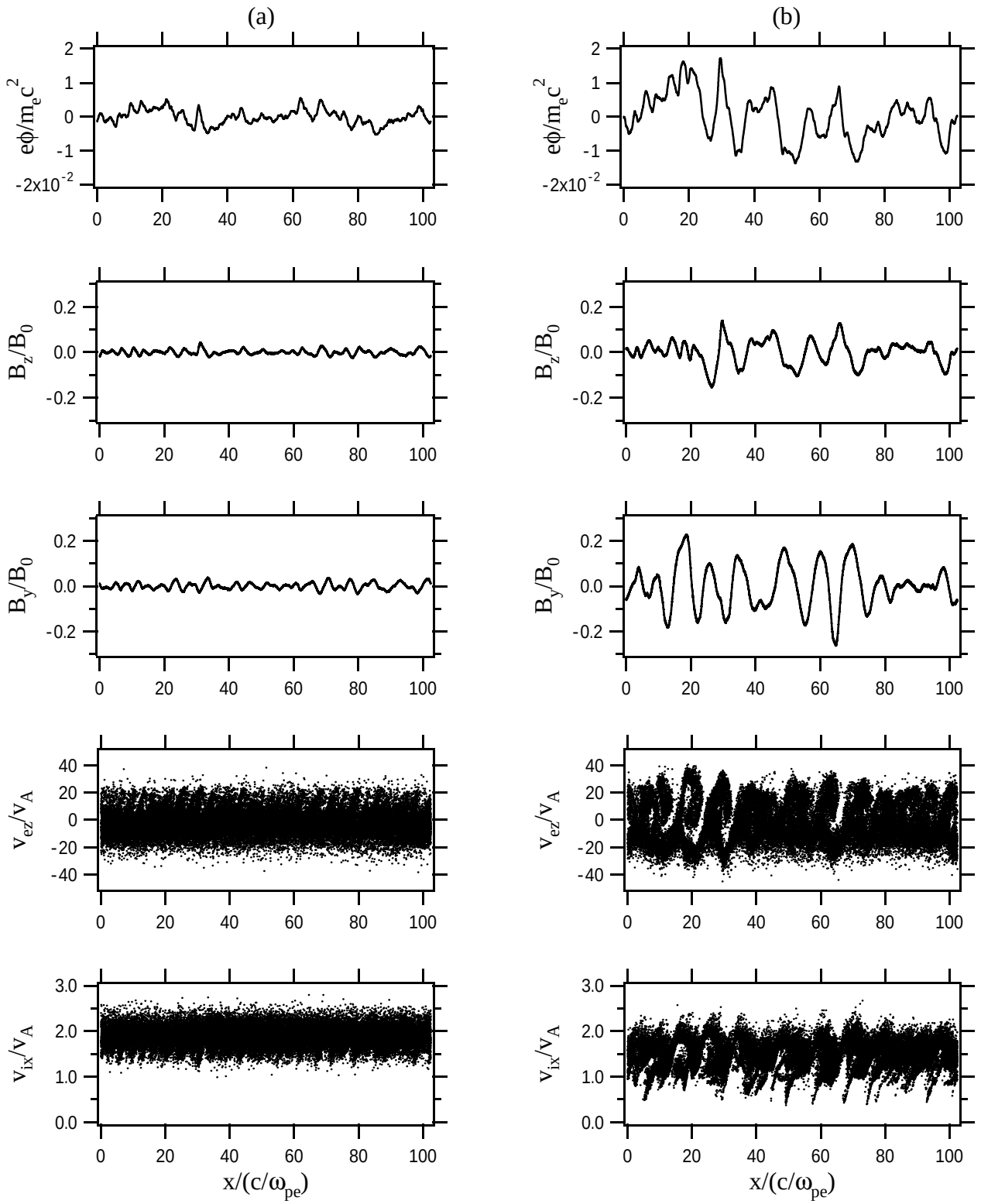
(a)
(b)
eϕ/m_ec^2
2
1
0
-1
-2x10^-2
B_z/B_0
0.2
0.0
-0.2
B_y/B_0
v_eZ/v_A
40
20
0
-20
-40
v_iX/v_A
3.0
2.0
1.0
0.0
0
20
40
60
80
100
x/(c/ω_pe)

Figure 11

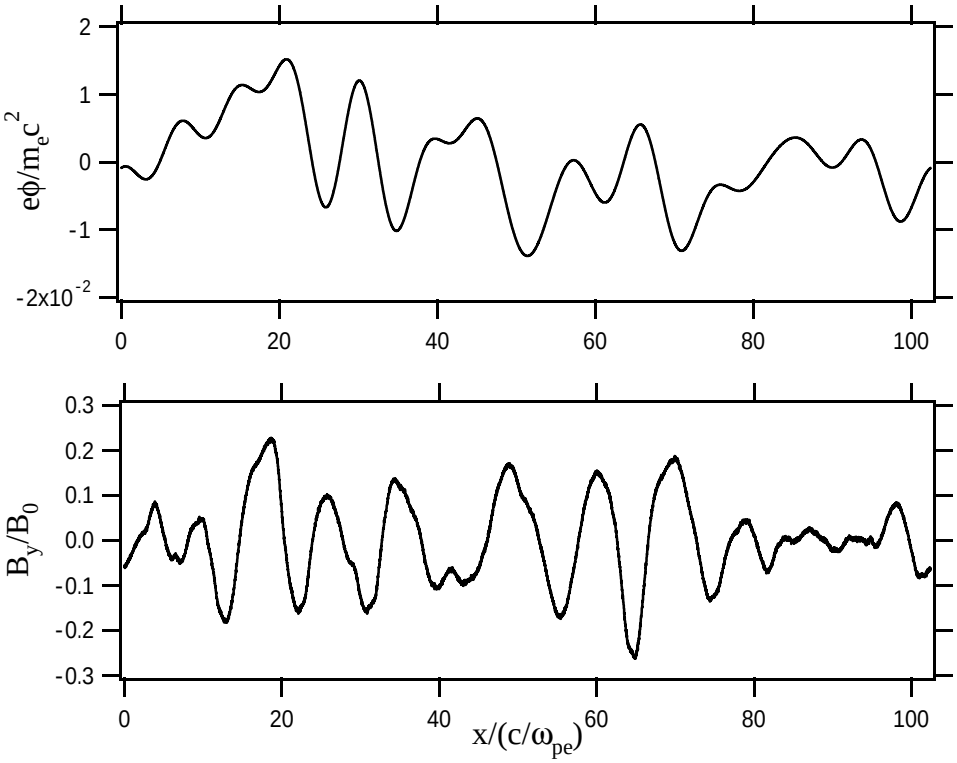
2
1
0
-1
-2x10^-2
eϕ/m_ec^2
0
20
40
60
80
100
0.3
0.2
0.1
0.0
-0.1
-0.2
-0.3
B_y/B_0
x/(c/ω_pe)

Figure 12